ELSEVIER

Contents lists available at ScienceDirect

Journal of Luminescence

journal homepage: www.elsevier.com/locate/jlumin



Full Length Article



Enhancing photoluminescence of manganese chloride perovskite-analogues through phase transformations induced by Sn incorporation

Qian Meng^a, Liuyun Chen^a, Liang Jing^a, Qi Pang^{a,*}, Jin Zhong Zhang^{b,**}

- ^a Guangxi Key Laboratory of Electrochemical Energy Materials/ School of Chemistry and Chemical Engineering, Guangxi University, Nanning 530004, Guangxi, People's Republic of China
- b Department of Chemistry and Biochemistry, University of California, Santa Cruz, CA 95064, USA

ARTICLE INFO

Keywords:

Manganese-based halide perovskite-analogue Phase transformations Photoluminescence Emission mechanism Light-emitting diode

ABSTRACT

Herein, we develop a facile strategy to synthesize one-dimensional Sn-incorporated CsMnCl $_3$ microcrystals (MCs) via an acid dissolution method under high humidity. The prepared CsMnCl $_3$ (H $_2$ O) $_\alpha$:0.50%Sn (α = 0 or 2, noted as CMCH:0.50%Sn) MCs exhibit an intense red emission assigned to 4 T $_{1g}$ → 6 A $_{1g}$ transition of Mn $^{2+}$ with a photoluminescence (PL) quantum yield (QY) of 15.77%, which is four times than that of pristine CsMnCl $_3$ (H $_2$ O) $_2$ MCs, with an activation energy of 160 meV determined from a temperature-dependent PL Boltzmann analysis. Sn $^{2+}$ ions incorporation can promote the formation of anhydrous CsMnCl $_3$ and are likely bonded to Cl ions. A red LED device based on CMCH:0.50%Sn MCs shows ultra-high color purity at a drive current of 300 mA and good stability. This work successfully addresses the issue of typically low PL QY of lead-free manganese halide perovskite-analogues (MHPAs) and provides insight into the fundamental optical properties and phase transformation mechanisms of all-inorganic MHPAs.

1. Introduction

Divalent manganese (Mn)-based halide perovskite-analogues (MHPAs), with a common formula A_nMnX_{n+2} (where A = alkali metal ions or large organic cations; X = Cl⁻, Br⁻ or I⁻), have emerged as a promising alternative to toxic lead-based halide perovskites [1,2] due to their strong light absorption capacity in the blue and ultraviolet (UV) regions, tunable luminescence from green to red, and large Stokes shifts [3,4]. Efficient MHPAs emitters, like C₄H₁₂NMnCl₃ [5], (BTPP)₂MnCl₄ [6], Cs₃MnBr₅ [7], and (ABI)₄MnBr₆ [8], have been successfully applied in light-emitting diode (LED), photoelectric sensor, X-ray imaging, and other fields. Nevertheless, the long photoluminescence (PL) decay lifetime (millisecond) of MHPAs remains an urgent problem that limits their superior practical applications [8,9]. Generally, the PL and associated decay dynamics in MHPAs governed by the ${}^{4}T_{1g} \rightarrow {}^{6}A_{1g}$ electron transition of Mn^{2+} with a $3d^5$ electron configuration are highly structure-dependent and primarily depend on the coordinated environment of Mn²⁺ [10]. Rodríguez and co-workers [11] found that when the tetrahedral-coordinated [(CH₃)₄N]₂MnCl₄ (green emission) is converted to the octahedral-coordinated [(CH₃)₄N]MnCl₃ (red emission), the PL decay lifetime of Mn²⁺ decreased by two orders of magnitude due to the decrease of the distance of Mn–Mn (d_{Mn-Mn}) and the increase of the crystal-field splitting, while the excitation and emission of Mn^{2+} are mainly affected by the strength of Mn–X bonds [3,11,12]. However, the existence of labile organic components in hybrid MHPAs is non-ideal for practical applications and the all-inorganic MHPAs commonly present a low PL quantum yield (QY). Therefore, it is vital to develop all-inorganic MHPAs with hexa-coordinated structures and optimize the coordinated environment of Mn^{2+} to improve their luminescence properties, then to fulfill the application demand in light-emitting devices.

CsMnCl₃ and its hydrate CsMnCl₃(H₂O)₂ have been widely studied as a typical example of one-dimensional (1D) Heisenberg antiferromagnetic materials in cryophysics but rarely reported as an all-inorganic perovskite-analogue optical functional material. Both of them exhibit a chain structure linked by hexagonal [MnX₆]⁴⁻ (X = Cl or OH) octahedral units. The distinction is that the [MnCl₄(OH)₂]⁴⁻ octahedron in CsMnCl₃(H₂O)₂ [*Pcca* (54)] is connected along the a-axis by sharing Cl atoms and forming O–H····Cl hydrogen bonds, while the [MnCl₆]⁴⁻ octahedron in CsMnCl₃ [$R\overline{3}m$ (166)] along the c-axis by sharing faces and angles without hydrogen bonds [13]. The loss of crystalline water reduces d_{Mn-Mn} from 4.563 Å to 3.156 Å, thus enhancing the crystal-field

E-mail addresses: pqigx@163.com (Q. Pang), zhang@ucsc.edu (J.Z. Zhang).

 $^{^{\}ast}$ Corresponding author.

^{**} Corresponding author.

splitting around Mn²⁺ and causing a redshift on the emission peak [14]. Therefore, CsMnCl₃(H₂O)₂ typically emits around 625-640 nm while CsMnCl₃ emits at a deeper red wavelength of 660-670 nm, which is useful for improving human vision [15]. Meanwhile, the PL lifetime of inorganic cesium manganese halides is 1-2 orders of magnitude shorter than that of most organic-inorganic hybrid manganese halides, and CsMnBr₃ nanocrystals have even been reported to possess a picosecond lifetime [2,13]. The deeper infrared fluorescence and shorter fluorescence decay lifetime of inorganic manganese halides are conducive to the fabrication of body-friendly red LED devices. However, during the preparation of CsMnCl₃, hydrate CsMnCl₃(H₂O)₂ impurities with a low PL QY are often spontaneously generated instead of CsMnCl₃ at ambient conditions. There is little research on phase transformations from CsMnCl₃(H₂O)₂ to anhydrous CsMnCl₃ by metal ions incorporation strategy. Designing efficient approaches to synthesize high-performing MHPAs is highly desired.

In this work, a facile synthesis of CsMnCl $_3$ (H $_2$ O) $_2$ microcrystals (MCs) was demonstrated via room-temperature acid dissolution recrystallization at ambient conditions with high relative humidity. The crystalline structural transformation from CsMnCl $_3$ (H $_2$ O) $_2$ MCs to anhydrous CsMnCl $_3$ MCs was realized by incorporating Sn $^{2+}$ ions. Therefore, the activation energy of the crystal increases and PL QY was enhanced to 15.77% due to Sn $^{2+}$ ions incorporation-induced CsMnCl $_3$ (H $_2$ O) $_2$ –CsMnCl $_3$ phase transition and crystal-field changes around Mn $^{2+}$. Furthermore, a red LED device based on Sn-incorporated powder was fabricated and showed stable luminous properties even at a high drive current.

2. Experimental section

2.1. Materials

All chemicals were used without further purification. Manganese (II) chloride tetrahydrate (MnCl $_2$ •4H $_2$ O, 99.99%), cesium chloride (CsCl, 99.99%), stannous chloride (SnCl $_2$, \geq 99.99%), stannous bromide (SnBr $_2$, \geq 99%), isopropyl alcohol (\geq 99.5%), and potassium bromide (KBr, \geq 99.5%) were purchased from Aladdin. Hydrochloric acid (36.0–38.0%) was purchased from Knowles of Chengdu Kelong Chemical Co., Ltd.

2.2. Synthesis

For pristine $CsMnCl_3(H_2O)_2$ MCs, 2.0 mmol $MnCl_2 • 4H_2O$ was dissolved entirely in 5.0 mL hydrochloric acid. CsCl (2.0 mmol) was then added to the precursor solution under vigorous stirring and rose pink sediments of $CsMnCl_3(H_2O)_2$ MCs were obtained immediately. After 10 min, the solution was centrifuged at 6000 rpm for 10 min. Finally, sediments were dispersed into isopropyl alcohol, washed twice, and fully ground after vacuum drying at 45 °C for 3 h. The whole process took place in Nanning, China, where the average relative humidity was above 80%.

Sn-incorporated MCs were synthesized by the identical approach, but the proper amount of $\rm SnCl_2$ or $\rm SnBr_2$ was added into the $\rm Mn^{2+}$ ions precursor solutions with nominal Sn/Mn atomic ratios (x%) as 0.25%, 0.50%, 0.75%, 1.00%, 1.25%, 1.50%, and 5.00%, respectively. With the content of Sn increasing, the sediments glowed bright red under 365 nm ultraviolet light and then weakened after reaching the maximum. The centrifugation and purification methods of the acquired solutions and sediments were the same as pristine $\rm CsMnCl_3(H_2O)_2~MCs.$

2.3. Structural and chemical characterization

X-ray diffraction (XRD) was carried out on a SmartLab3KW powder diffractometer using Cu K α radiations source at 40 kV and 30 mA. Raman spectra were measured with a LabRAM HR Evolutions instrument of HORIBA Jobin Yvon using a 532 nm laser source. Electron

paramagnetic resonance (EPR) spectrum was obtained at X-band on a Bruker-A300-10/12 spectrometer at room temperature. Field emission scanning electron microscope (FESEM) images were taken using a Quanta 450 FEG microscope of FEI at an accelerated voltage of 20 kV (gold-sprayed before the test). Transmission electron microscopy (TEM) and high-resolution TEM (HRTEM) images were measured using a JEOL JEM-2100 Plus operating at an acceleration voltage of 200 kV, equipped with a sensitive TVIPS (XF416) CMOS camera. Energy disperse spectroscopy (EDS) element imaging, and mapping analyses were carried out on an Oxford X-MAX 80 microscope, with sample solutions dropped on 200 mesh copper mesh. X-ray photoelectron spectroscopy (XPS) was measured with Thermal Fisher Escalab 250Xi spectrometer. Inductively coupled plasma optical emissions spectrometer (ICP-OES) analyses were performed by Agilent 730, and the Fourier Transform Infrared (FT-IR) spectra were conducted using a TENSOR II of Bruker using the KBr pellet technique (after being dried completely) with the wavenumber range of $400-3700 \text{ cm}^{-1}$.

2.4. Optical measurements

Ultraviolet–visible diffuse reflection (UV–vis DRS) electronic absorption spectra were recorded with a Techcomp UV2600 variable slit UV–vis spectrophotometer equipped with an integrating sphere. Steady-state PL spectra and PL excitation (PLE) spectra were measured using an FLS1000 spectrofluorometer of Edinburgh Instruments with a Xenon lamp (450 W). Absolute PL QY was determined by employing a barium sulfate-coated integrating sphere (Edinburgh). Time-resolved PL (TRPL) data were collected on an Edinburgh $\mu F2$ lamp for μs lifetime measurements, and the TRPL decay curves of Mn^{2+} emission were fit with a single exponential function:

$$I(t) = A e^{-\frac{t}{\tau}} \tag{1}$$

where A is the amplitude and τ represents the decay lifetime. For temperature-dependent PL measurements, the samples were put inside an Oxford Instruments OptistatDN-V cryostat with a tunable temperature range from 100 to 400 K. Photographs of the samples were taken under 365 nm UV excitation without using any filter.

2.5. Fabrication of LED

50 mg 0.50%Sn-incorporated MCs powder was mixed with ZWL8820 organic silica gel at a powder/gel ratio of 0.3:1. The mixture was then coated on a commercial 370 nm GaN UV chip of San'an Optoelectronics Co., Ltd. for the capsulation of the LED device. Parameters of the device were reported using an HP9000 LED spectrum analyzer with an operating current ranging from 20 to 300 mA.

3. Results and discussion

Pristine CsMnCl₃(H₂O)₂ MCs were synthesized via a facile method in hydrochloric acid at room temperature with an average relative humidity of over 80%, following the modified procedure [16]. We introduced additional SnCl₂ to the precursor solution of Mn²⁺ ions with the molar ratio (x%) of Sn to (Sn + Mn) set to 0.25%-5.00%. All peaks in the XRD pattern of the pristine sample shown in Fig. 1(a) can be indexed to CsMnCl₃(H₂O)₂ (ICSD 24083) parameters with orthorhombic phase structure [14] without discernible impurity peaks. With the introduction of SnCl₂, a set of peaks assigned to (105), (110), (204), and (205) crystalline planes can be observed, which are representative of the trigonal CsMnCl₃ (ICSD 21105) phase [17], and the prepared product was converted to a mixture of CsMnCl₃(H₂O)₂ and CsMnCl₃. The mixture was redefined as $CsMnCl_3(H_2O)_{\alpha}$:x%Sn ($\alpha = 0$ or 2, noted as CMCH:x%Sn) MCs. When x was less than 1.00, the strongest characteristic peak at 30.7° was attributed to (122) plane of CsMnCl₃(H₂O)₂, while the strongest diffraction peak at 24.4° was ascribed to (110) plane

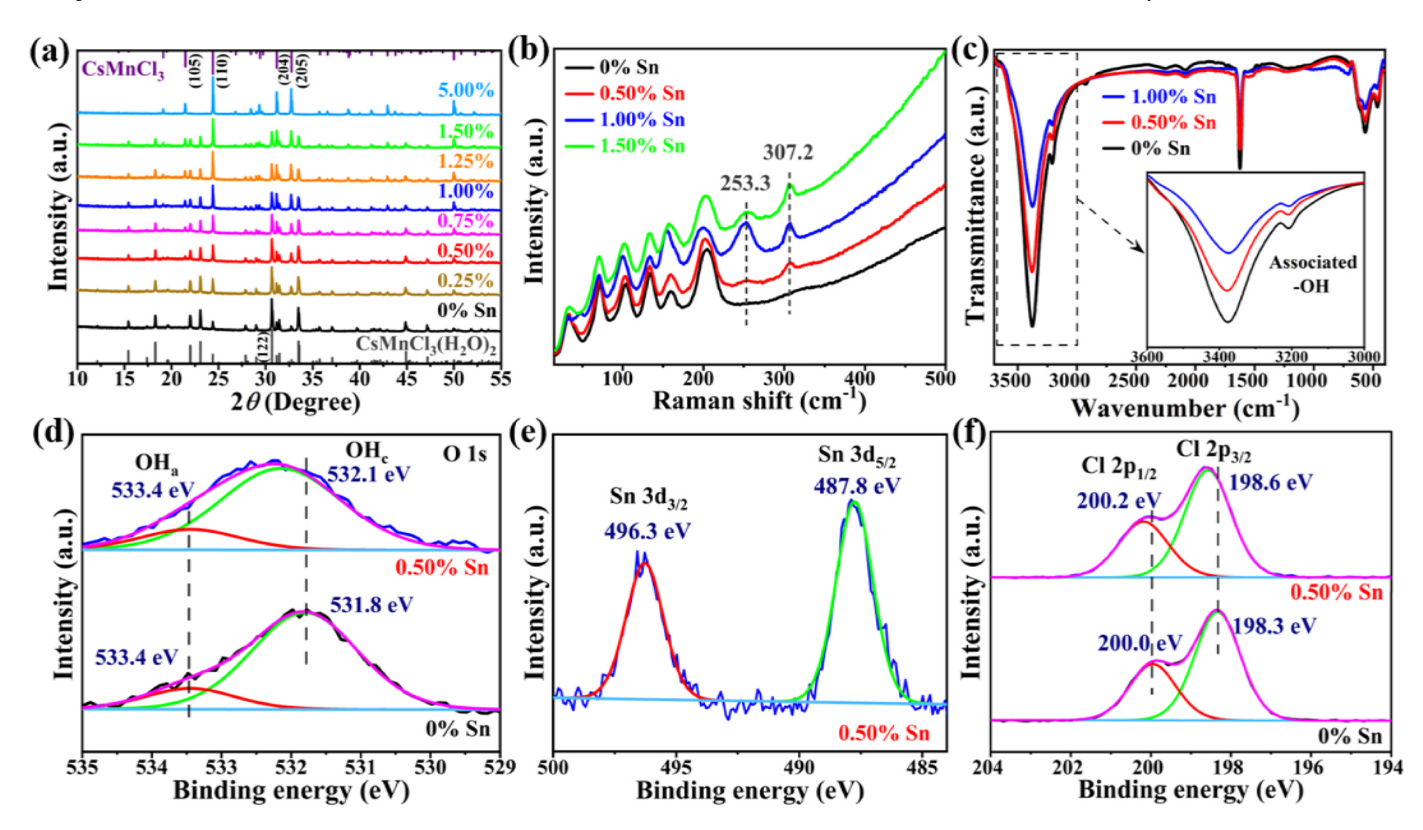


Fig. 1. (a) XRD patterns, (b) Raman spectra, (c) FT-IR spectra (the insert shows magnified IR peaks of the associated hydroxyl group), high-resolution XPS spectra of (d) O, (e) Sn, and (f) Cl of samples with and without Sn incorporation.

of CsMnCl $_3$ when x reached 1.00. Therefore, CsMnCl $_3$ becomes the major crystalline phase at x = 1.00 or above. When the incorporation amount of Sn reaches 5.00%, the pure phase of CsMnCl $_3$ was observed, indicating that a higher concentration of Sn ions can promote the formation of anhydrous CsMnCl $_3$ MCs effectively. Since the reaction was carried out in a Cl-rich hydrochloric acid environment, the influence of the Cl component of SnCl $_2$ on the reaction environment can be ignored, which will be demonstrated later. During this process, there is only a slim chance that the introduced Sn ions are doped and replace the Mn of CsMnCl $_3$ (H $_2$ O) $_2$ since there is no observable change in the lattice constants. The concentration of Sn $^{2+}$ ions in the final products of CMCH:x% Sn MCs was measured by ICP-OES (Table S1). For CMCH:0.50%Sn MCs, the content of Sn ions was determined to be 0.37%.

To further monitor the evolution of crystal structure before and after incorporating Sn ions, we used Raman spectroscopy to study the samples with a 532 nm laser, with results shown in Fig. 1(b). Peaks at 34.2, 71.1, 104.0, 134.2, 159.7, and 204.3 cm $^{-1}$ are identified as characteristic vibration peaks of CsMnCl $_3$ (H $_2$ O) $_2$, identical to the results reported in literature formerly [18,19]. However, for Sn-incorporated samples, extra peaks appear at 253.3 cm $^{-1}$ and 307.2 cm $^{-1}$. The signal at 253.3 cm $^{-1}$ can be attributed to symmetric stretching and deformation vibration of Sn–Cl [20,21], while the signal at 307.2 cm $^{-1}$ is derived from the strong chemisorption of Sn species [22,23]. Raman results show that the introduced Sn ions may be bonded to the Cl ions in the prepared MCs. We suggest that the incorporated Sn ions hinder the formation of O–H····Cl hydrogen bonds and inhibit the interaction between crystalline water and [MnCl $_6$] $^{4-}$ octahedron in CsMnCl $_3$ (H $_2$ O) $_2$, and thus facilitate the formation of the CsMnCl $_3$ crystalline phase.

Furthermore, we conducted an FT-IR study for a qualitative analysis of the content changes of crystalline water in the samples before and after Sn ion incorporation (Fig. 1(c)). A broad and strong absorption band related to the stretching vibration of water molecules was observed in the high frequency infrared spectral area (3600–3000 $\rm cm^{-1}$), which exhibits two absorption peaks at 3366 $\rm cm^{-1}$ and 3244 $\rm cm^{-1}$. These two

peaks can be identified as the characteristic peaks of the crystalline water molecules [24]. In contrast, the characteristic peaks of the free water molecules appear around 3429 cm $^{-1}$ and 3475 cm $^{-1}$ [24]. The sharp and strong peak observed at 1624 cm $^{-1}$ is attributed to the in-plane bending vibration of the O–H bonds of water molecules, while the weaker peaks at 622 cm $^{-1}$, 568 cm $^{-1}$, and 465 cm $^{-1}$ are assigned to the out-of-plane bending vibration of O–H bonds [24,25]. It is evident that with the increase in the amount of incorporated Sn ions, the intensity of infrared absorption peaks of crystalline water in the samples decreases continuously, confirming that the Sn ion incorporation has a practical inhibition effect on the formation of CsMnCl₃(H₂O)₂ MCs under high relative humidity.

The chemical composition and electronic characteristics of O, Sn, and Cl elements in pristine and Sn-incorporated samples were studied via XPS (Fig. 1(d-f)). The O 1s spectrum of CsMnCl₃(H₂O)₂ MCs in Fig. 1 (d) can be fitted by Gaussian fitting at 533.4 eV and 531.8 eV, corresponding to hydroxy-O of surface adsorption water (OHs) and crystalline water (OH_c), respectively [26-28]. Notably, the OH_c peak shifts to the higher binding energy of 532.1 eV while the OHs peak remains unchanged with the introduction of Sn ions. In the meantime, compared with pristine CsMnCl₃(H₂O)₂ MCs, two peaks of CMCH:0.50%Sn MCs appear at 496.3 eV and 487.8 eV in Fig. 1(e), attributed to Sn 3d_{3/2} and Sn $3d_{5/2}$, confirming the effective incorporation of Sn ions [21]. Fig. 1(d) and (e) suggest that the interaction between crystalline water and [MnCl₆]⁴⁻ weakens and Sn incorporation can restrain the procedure of crystalline water for CsMnCl₃(H₂O)₂ MCs with effect. Moreover, as shown in Fig. 1(f), with the incorporation of Sn, the peaks of ${\rm Cl}\,2p_{1/2}$ and Cl 2p_{3/2} shift by 0.2 and 0.3 eV in the direction of high binding energy, indicating the strong interaction between Sn and Cl ions, which corresponds to the results of Sn-Cl bonds in Raman spectra. Although the lattice constant in the XRD patterns had no significant shift after Sn incorporation, the possibility that Sn replaced Mn in the crystal lattice cannot be ruled out. In addition, the shift of the Cl 2p peak might also be caused by the absence of crystalline water in CMCH:0.50%Sn MCs.

Based on the above analysis, a proposed crystal growth mechanism and schematic diagram of the atomic structure of CMCH:x%Sn were drawn in Fig. S1. Besides, Table S2 lists the atomic ratios of elements on the surface of CMCH:0.50%Sn MCs obtained by XPS, and the proportion of Sn atom is 0.52%. Furthermore, we investigated the surrounding environment of Mn²⁺ ions in CMCH:0.50%Sn MCs via X-band EPR spectrum. As shown in Fig. S2, the EPR spectrum shows one broad formant from divalent manganese centers rather than distinct six-fold hyperfine splitting peaks [29], which is caused by severe d-electron spin relaxation of Mn–Mn magnetic coupling in the MCs since MHPAs are generally expected to be paramagnetic materials at room temperature [13,30,31].

The pristine CsMnCl $_3$ (H $_2$ O) $_2$ MCs show poor crystallinity and irregular morphology in the SEM images (Fig. 2(a)), with a grain size of about 0.7–1.0 μ m and non-uniform grain distribution. Some grains agglomerate together to form massive block particles. After the Sn ion incorporation, as shown in Fig. 2(b) and (c), when x=0.50%, in addition to small-sized particles similar to CsMnCl $_3$ (H $_2$ O) $_2$ MCs, additional large-sized rhombohedral particles with a diameter of about 2.5–3.5 μ m appear, which are the newly generated CsMnCl $_3$ MCs consistent with the XRD result. When x rises to 1.50%, rhombohedral particles account for the primary phase, while small-sized CsMnCl $_3$ (H $_2$ O) $_2$ MCs particles disperse around them. According to the HRTEM image of Fig. 2(d–f), there are lattice fringes with a spacing of 0.291 nm in the samples x = 0%, 0.50%, and 1.50%, in accord with the (122) planes of the orthogonal CsMnCl $_3$ (H $_2$ O) $_2$ crystal. With the increase of Sn ion amount,

spacing of 0.288 nm (x = 0.50%) and 0.274 nm (x = 1.50%) are observed, corresponding to (204) and (205) crystalline planes of tripartite CsMnCl₃ crystal, respectively. The information obtained by SEM and HRTEM images is in line with XRD data, suggesting that the crystal structure of CsMnCl₃(H₂O)₂ MCs transforms into the second crystalline phase of CsMnCl₃ MCs via Sn incorporation. Atomic EDS-mapping images of CMCH:0.50%Sn MCs indicate uniform distributions of Cs, Mn, Cl, O, and Sn elements (Fig. 2(g-1)). The presence of Sn ions is further confirmed as an atomic percentage of 0.42% (Table S2).

UV–vis absorption spectra of the pristine and Sn-incorporated samples in Fig. 3(a) show semblable absorption peaks representing the $d\!-\!d$ electron transition of Mn $^{2+}$ ions. However, after Sn ion incorporation, the loss of crystalline water shortens d_{Mn-Mn} and increases the strength of the crystal-field splitting around Mn^{2+} ions resulting in a strong coupling optical conversion between $Mn^{2+}-Mn^{2+}$, which enhances the absorption intensity of CMCH:Sn MCs and causes a slight red shift of 4 nm [14]. Due to the low spin-forbidden in Mn octahedral coordination ([MnX₆] $^{4-}$), the $^6A_{1g} \rightarrow ^4T_{1g}$ transition band (near 540 nm) makes CsMnCl₃(H₂O)₂ MCs a broad red PL emission band (FWHM \sim 97 nm, λ_{ex} = 417 nm) at 638 nm, as shown in Fig. 3(b) [32,33]. Whereas the intense Mn–Mn crystal-field splitting of CMCH:Sn MCs causes the emission band to redshift to 660 nm (λ_{ex} = 420 nm) with an FWHM of \sim 93 nm while the peak symmetry shows no obvious change. Surprisingly, thanks to the ideal proportion of CsMnCl₃ and CsMnCl₃(H₂O)₂ and the passivation effect of the incorporated Sn ions, the PL intensity of samples with Sn

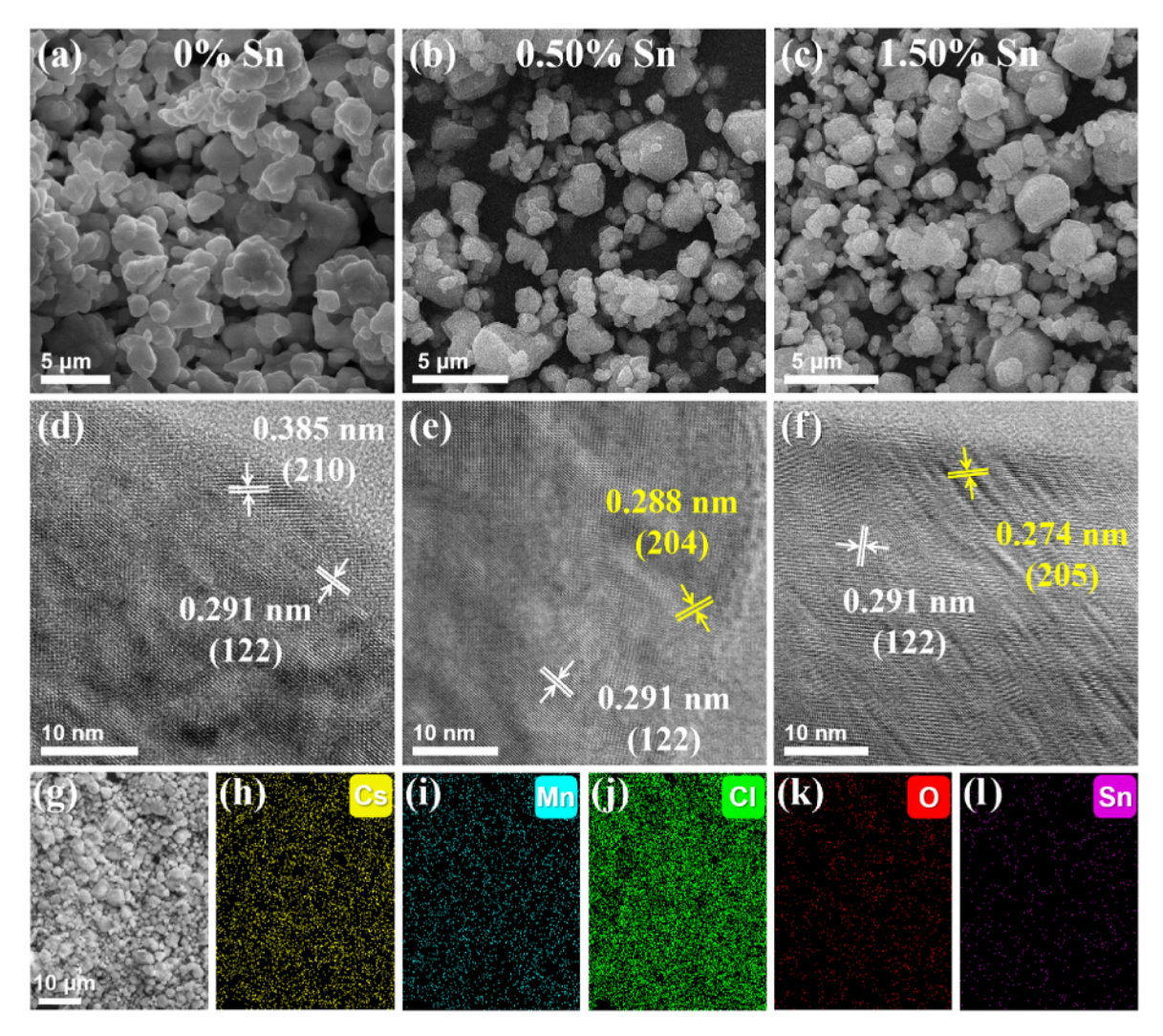


Fig. 2. SEM and HRTEM images of samples with (a, d) 0% Sn, (b, e) 0.50% Sn and (c, f) 1.50% Sn. (g-l) Atomic EDS-mapping images of the sample with 0.50% Sn.

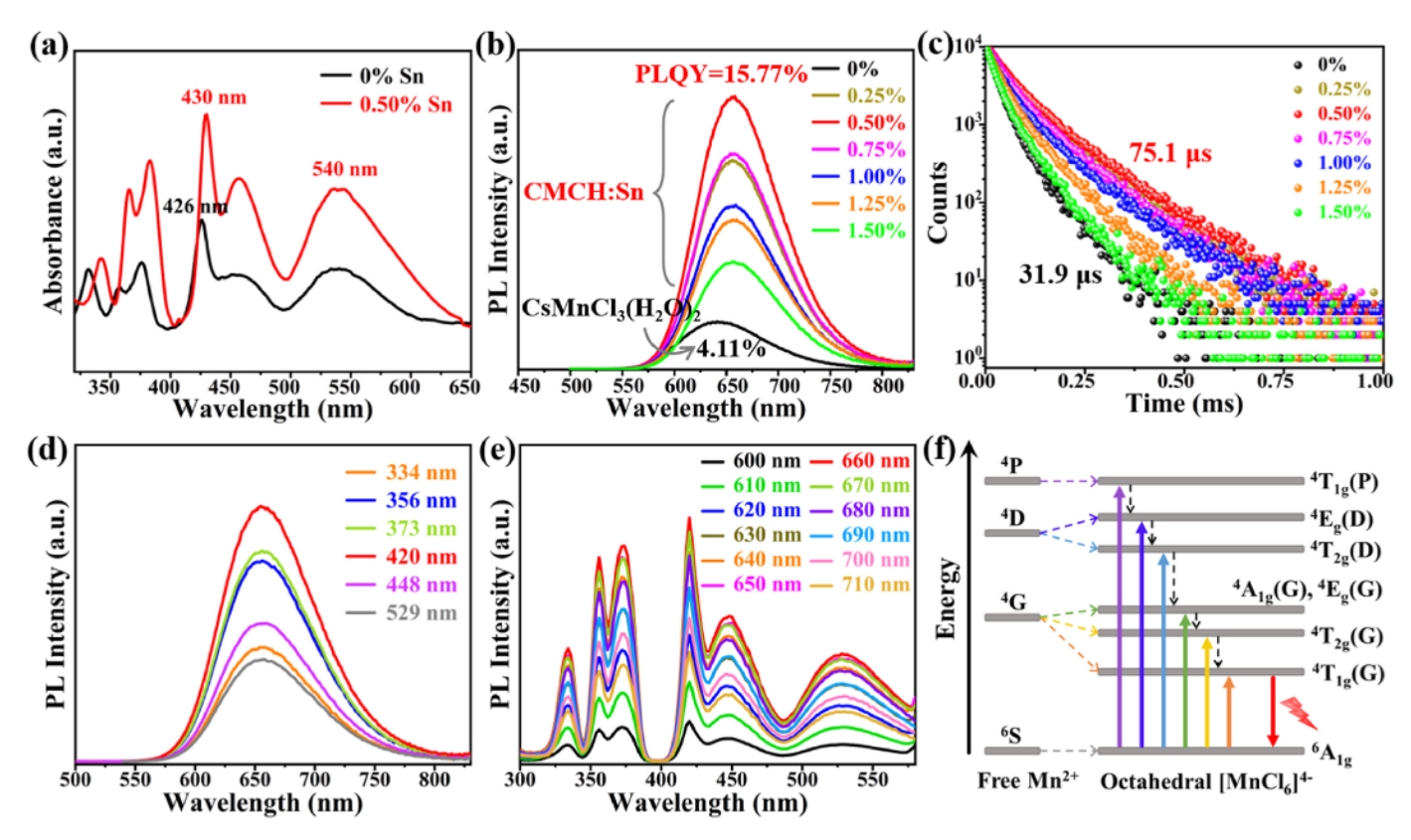


Fig. 3. (a) UV–vis absorption spectra, (b) PL spectra (CsMnCl₃(H₂O)₂: $\lambda_{ex} = 417$ nm, CMCH:x%Sn: $\lambda_{ex} = 420$ nm), and (c) TRPL decay curves (CsMnCl₃(H₂O)₂: $\lambda_{em} = 638$ nm, CMCH:x%Sn: $\lambda_{em} = 660$ nm) of samples with different x% Sn. (d) Emission-wavelength-dependent PL spectra, (e) excitation-wavelength-dependent PLE spectra, and (f) energy level diagram for d–d transitions and the PL emission from the free and octahedrally coordinated Mn²⁺ of CMCH:0.50%Sn MCs.

ions is remarkably improved, and we obtain the maximum emission when the molar ratio of Sn ions reaches 0.50%. The absolute PL QY rises from 4.11% (pristine) to 15.77% (Sn-incorporated), achieving a nearly four-fold enhancement. Meanwhile, such a large Stokes shift indicates that the self-absorption of CMCH:Sn MCs is negligible and favorable for its practical application to light-emitting devices [8].

TRPL was performed to clarify the influence of Sn ion incorporation on optical properties and dynamics. The TRPL decay profiles for Mn²⁺ emission shown in Fig. 3(c) are can be fit with a single exponential function, and the PL lifetime parameters are summarized in Table S3. The observed decay lifetime ($\tau_{\rm obs}$) derived from the $^4T_{1g}$ — $^6A_{1g}$ transition of samples is on the time scale of microsecond and the lifetime of pristine CsMnCl₃(H₂O)₂ MCs is 31.9 µs. The latter increases with the incorporation of Sn ions, reaching the maximum of 75.1 µs at x = 0.50% with the highest PL QY, and then decreases. Based on the PL QY and $\tau_{\rm obs}$, we can evaluate the radiative lifetime ($\tau_{\rm r}$) and non-radiative lifetime ($\tau_{\rm nr}$) of samples using the following equations [19,34]:

$$PLQY = \frac{\tau_{obs}}{\tau_r} \tag{2}$$

$$\frac{1}{\tau_{obs}} = \frac{1}{\tau_r} + \frac{1}{\tau_{nr}} \tag{3}$$

Calculated lifetime results are listed in Table 1. The Sn ion incorporation affects both the intrinsic electronic band structure (related to

 $\begin{tabular}{ll} \textbf{Table 1} \\ \textbf{Calculated radiative and non-radiative lifetimes for pristine and Sn-incorporated samples.} \\ \end{tabular}$

Samples	$\tau_{ m obs}$ (μs)	τ_{r} (µs)	$\tau_{ m nr}$ (μ s)	PL QY
CsMnCl ₃ (H ₂ O) ₂	31.9	776.2	33.3	4.11%
CMCH:0.50%Sn	75.1	476.2	89.3	15.77%

radiative decay, from 476.2 μs to 776.2 μs) and extrinsic defect trap states (related to non-radiative decays, from 33.3 μs to 89.3 μs). On one hand, more water molecules in CsMnCl₃(H₂O)₂ MCs give them "softer" lattice characteristics and higher vibration frequency under photoexcitation than CsMnCl₃ MCs, which generally results in a faster τ_{obs} [13, 35]. On the other hand, the appearance of a shorter τ_{r} and a longer τ_{nr} usually manifests that non-radiative decays are restrained, availing of the radiative recombination and leading to a high PL QY [36]. We suggest that appropriate Sn ion incorporation helps to passivate Cl defect sites in the lattice and inhibit the non-radiative pathway to reduce energy loss and higher PL QY.

To investigate the underlying mechanism of the aforementioned emission behavior in CMCH:0.50%Sn MCs, we employed different excitation wavelengths for PL measurements. As shown in Fig. 3(d), no shift is found in the PL emission band with excitation wavelength changing from 334 to 529 nm. The independence of PL spectra to excitation wavelength confirms that the red emission of CMCH:0.50%Sn MCs originates from the same Mn^{2+} ion ${}^4T_{1g} \!\!\!\!\! \to {}^6A_{1g}$ excited state relaxation as pristine octahedrally coordinated Mn-based perovskite-analogues [16]. At the same time, we can intuitively visualize six excitation peaks stem from the d-d electron transitions in Mn²⁺ ions from Fig. 3 (e), corresponding to the absorption bands in Fig. 3(a) [2]. The relevant energy levels and PL emission from the free and octahedrally coordinated Mn²⁺ of CMCH:Sn MCs are shown in Fig. 3(f). Peaks located at 335, 356, 374, 420, 448, and 529 nm in the PLE spectra are the results of electron transitions from the ground state ⁶A₁(⁶S) to excited states ${}^{4}T_{1g}({}^{4}P), {}^{4}E_{g}({}^{4}D), {}^{4}T_{2g}({}^{4}D), [{}^{4}A_{1g}({}^{4}G), {}^{4}E_{g}({}^{4}G)], {}^{4}T_{2g}({}^{4}G), and {}^{4}T_{1g}({}^{4}G),$

In addition, as a control experiment, CMCH:SnBr $_2$ MCs were synthesized with SnBr $_2$ used to introduce Sn ions into CsMnCl $_3$ (H $_2$ O) $_2$ MCs. Their luminescent properties and surface chemical composition were measured as shown in Fig. S3. Changes in PL and TRPL spectra before

and after the introduction of $SnBr_2$ are similar to that of introducing $SnCl_2.$ When the molar ratio of $SnBr_2$ is 0.50%, the sample reaches the highest absolute PL QY (14.95%) and the longest $\tau_{\rm obs}$ (74.6 μs) with a $\lambda_{\rm ex}$ of 420 nm and a $\lambda_{\rm em}$ of 660 nm, similar to the sample of CMCH:0.50%Sn prepared with $SnCl_2$, proving the effective incorporation and passivation of $SnBr_2$ on $CsMnCl_3(H_2O)_2$ MCs. In the XPS spectra of CMCH:0.50% $SnBr_2$ MCs, two peaks of Sn 3d at 496.2 eV and 487.7 eV appear, while no signal of Br 3d could be detected. The results manifest that only Sn ions can successfully incorporate into $CsMnCl_3(H_2O)_2$ MCs and passivate the Cl defects in the lattice, acting as a brake for the formation of crystalline water.

We found major differences between the temperature-dependent PL spectra of CsMnCl₃(H₂O)₂ MCs and CMCH:0.50%Sn MCs, with the temperature varying from 100 to 440 K, as shown in Fig. 4. Both the PL intensities of the samples decrease with elevating temperature under 300 K because of the thermal quenching effect caused by the increasing dynamic thermal vibration [37,38], and a blue shift occurs due to the crystalline lattice expansion and the weakened crystal-field splitting strength [13]. Further elevating the temperature from 300 to 440 K, the PL intensity of pristine CsMnCl₃(H₂O)₂ MCs ($\lambda_{ex} = 417$ nm) begins to rebound, and the PL wavelength shows an apparent redshift, which is ascribed to the enhancement of the crystal-field splitting strength of Mn–Mn led by the loss of crystalline water and the phase transformation from CsMnCl₃(H₂O)₂ MCs to CsMnCl₃ MCs at high temperature [14]. The FWHM of the emission bands shows a broadening trend, which is ascribed to an increasing number of higher vibration levels for the excited state of ⁴T_{1g} with elevating the temperature [13,39]. When the temperature reaches 400 K, the thermal quenching effect becomes the dominant factor again, bringing a continuous decline in PL intensity. However, for CMCH:0.50%Sn MCs ($\lambda_{ex} = 420$ nm), the PL intensity merely possesses a monotonic downward trend with a broadened FWHM showing no sign of phase transition, and the PL wavelength shifts from 670 nm (100 K) to 658 nm (440 K) due to the lattice thermal expansion. Simultaneously, as the aforementioned phenomenon that the PL bands showed no apparent shift or change in the peak symmetry at x = 0.25-1.50, it suggests that the PL bands of CMCH:0.50%Sn MCs at 660nm are mainly derived from CsMnCl3 rather than CsMnCl3(H2O)2, and the contribution of CsMnCl₃(H₂O)₂ MCs to the PL at 660 nm is very slight.

The activation energies (E_a) of CsMnCl₃(H₂O)₂ MCs and CMCH:0.50%Sn MCs are calculated by the following Arrhenius formula using temperature-dependent PL spectra data [6,39–41]:

$$I(T) = \frac{I_0}{1 + Ae^{-\frac{E_0}{k_B T}}} \tag{4}$$

where I(T) and I_0 represent the integrated PL intensity at the experimental temperature T (K) and 0 K k_B represents the Boltzmann constant, and A is a constant. As a result, the E_a value of pristine CsMnCl₃(H₂O)₂ MCs is calculated to be ~107 meV (100–300 K) while that of CMCH:0.50%Sn MCs is approximately 160 meV (100–440 K) which is heightened by nearly 50%, indicating that the excited electrons generated in CMCH:0.50%Sn MCs are more difficult to overcome the energy barrier for the non-radiative transition but more possible to recombine directly. This corresponds to the faster radiation recombination lifetime of CMCH:0.50%Sn MCs [39]. The results explain the enhancement of PL QY after Sn ion incorporation and clarify the non-negligible role of Sn ions in the system. It shows simultaneously that it is beneficial to the application of red light-emitting devices.

Although Mn-based perovskite-analogues exhibit more intense excitation bands at blue wavelength, the commercial lighting industry is moving towards a higher drive current. Compared with blue LED chips, near-UV LED chips possess lesser current attenuation and better performance at higher drive currents [42]. CMCH:0.50%Sn MCs powder was mixed with organic silica gel and coated on a 370 nm near-UV GaN chip to fabricate a red LED device to verify its application potential in solid-state lighting. Fig. 5(a) shows the PL spectra ($\lambda_{ex}=370$ nm) and lists the chromaticity coordinates and correlated color temperature (CCT) parameters of the fabricated device at drive currents in 20-300 mA. It can be observed that the PL intensity at ~655 nm increases steadily with the ascent of the drive current, and the PL band shape and position exhibit no distinct change, projecting quite excellent luminescence stability [39]. Chromaticity coordinates in CIE 1931 system are drawn in Fig. 5(b). By raising the drive current from 20 mA to 300 mA, the luminous efficiency of the device is improved from 10.67 lm W⁻¹ to 11.21 lm W⁻¹, and the color rendering index goes up from 23.3 to 38.4 with the color purity remaining at 99.9%, which ensures the stable luminous property of the red LED device under high drive currents. The illustration in Fig. 5(c) presents photos of the LED device based on CMCH:0.50%Sn MCs operating under indoor natural light (left) and a 20 mA drive current (right), and bright red light emitted by the device is in sight under operating conditions. These results demonstrate the potential of efficient and stable red LED devices based on CMCH:Sn MCs.

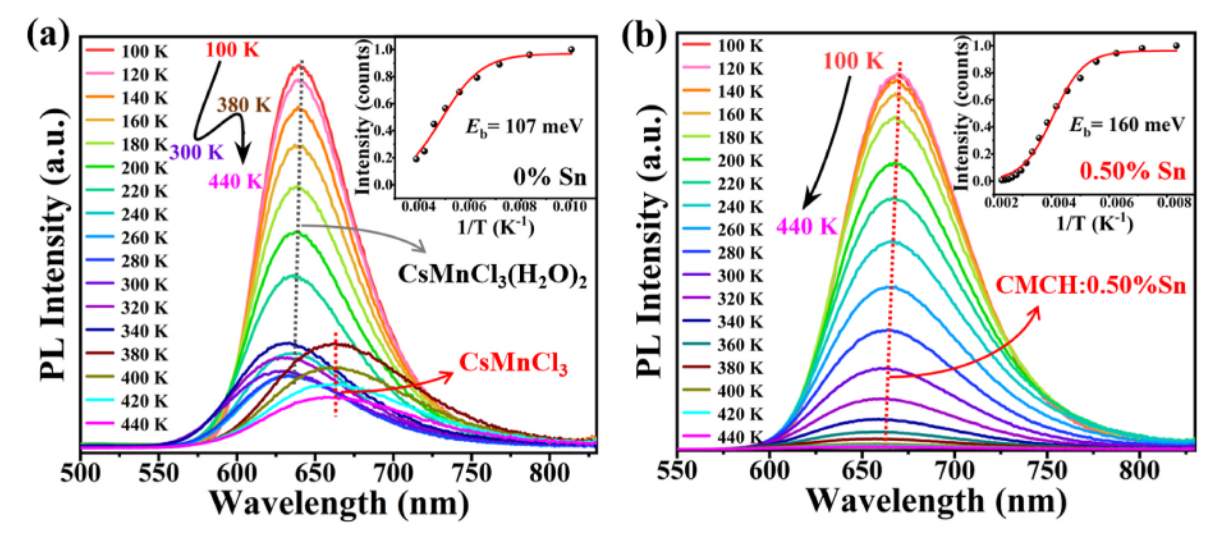


Fig. 4. Temperature-dependent PL spectra of (a) CsMnCl₃(H₂O)₂ MCs ($\lambda_{ex}=417$ nm) and (b) CMCH:0.50%Sn MCs ($\lambda_{ex}=420$ nm) in the temperature range of 100–440 K. Inserts: Boltzmann analyses of PL intensity vs T.

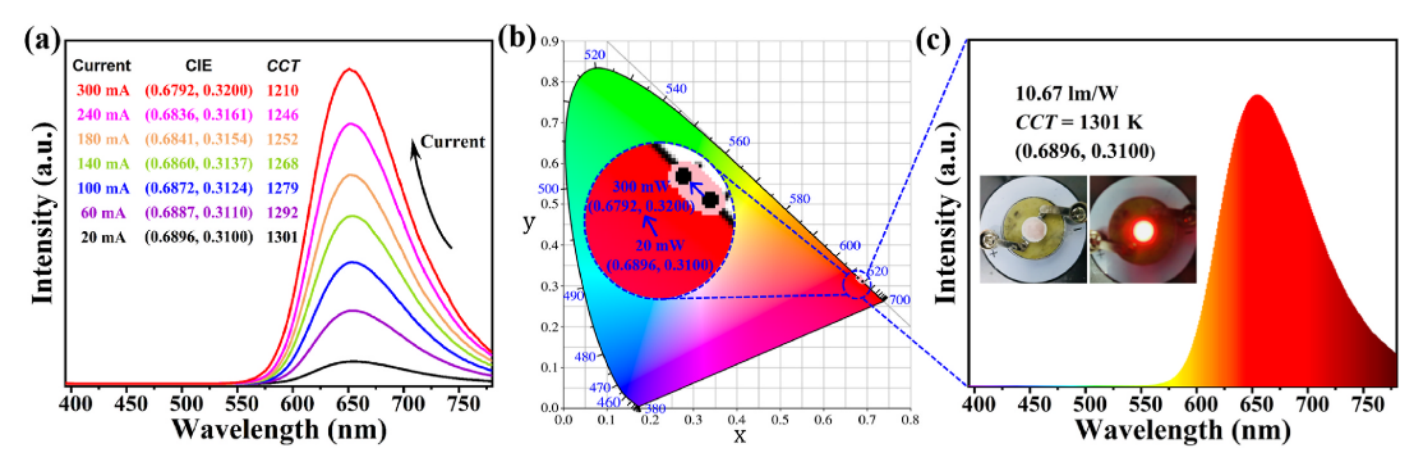


Fig. 5. (a) PL spectra ($\lambda_{\rm ex} = 370$ nm) under different driving currents from 20 to 300 mA, (b) chromaticity coordinates (black dots) in the CIE 1931 system, and (c) PL spectrum and photographs of the fabricated LED device based on CMCH:0.50%Sn MCs and a 370 nm near-UV chip.

4. Conclusions

In summary, we employed a facile Sn ions incorporation strategy to control the crystalline phase transformations between CsMnCl₃(H₂O)₂ MCs and CsMnCl₃ MCs under high relative humidity. The results from XRD, Raman, XPS, and FT-IR indicate that Sn ions are likely bonded to the Cl ions in the CsMnCl₃ MCs. This prevents the interaction between crystalline water and [MnCl₆]⁴⁻ octahedron in CsMnCl₃(H₂O)₂ MCs by blocking the formation of O-H····Cl hydrogen bonds, thus inducing the formation of CsMnCl₃ MCs. Due to the high lattice symmetry and crystal-field splitting strength of CsMnCl₃ MCs, the sample with 0.50% Sn incorporation possesses an activation energy of 160 meV, and a red emission with PL QY of 15.77%, nearly fourfold enhanced than the pristine CsMnCl₃(H₂O)₂ MCs. The red LED device based on CMCH:0.50%Sn MCs showed stable luminescence performance and ultra-high color purity at a high drive current, showing promise of all-inorganic manganese halide perovskite-analogues for LED applications.

Credit author statement

Qian Meng: Conceptualization, Methodology, Validation, Formal analysis, Investigation, Writing - Original Draft. Liuyun Chen: Formal analysis, Investigation. Liang Jing: Validation, Investigation. Qi Pang: Conceptualization, Methodology, Resources, Writing - Review & Editing, Supervision, Project administration, Funding acquisition. Jin Zhong Zhang: Writing - Review & Editing, Supervision, Funding acquisition.

Declaration of competing interest

The authors declare that they have no known competing financial interests or personal relationships that could have appeared to influence the work reported in this paper.

Data availability

Data will be made available on request.

Acknowledgments

This work was supported by the National Natural Science Foundation of China (Grant No. 21965003). JZZ acknowledges the U S NSF (CHE-2203633) for financial support.

Appendix A. Supplementary data

Supplementary data to this article can be found online at https://doi.org/10.1016/j.jlumin.2022.119613.

References

- [1] H. Bahmani Jalali, A. Pianetti, J. Zito, M. Imran, M. Campolucci, Y.P. Ivanov, F. Locardi, I. Infante, G. Divitini, S. Brovelli, L. Manna, F. Di Stasio, Cesium manganese bromide nanocrystal sensitizers for broadband vis-to-NIR downshifting, ACS Energy Lett. 7 (2022) 1850–1858, https://doi.org/10.1021/acsenergylett.2c00311.
- [2] J. Almutlaq, W.J. Mir, L. Gutiérrez-Arzaluz, J. Yin, S. Vasylevskyi, P. Maity, J. Liu, R. Naphade, O.F. Mohammed, O.M. Bakr, CsMnBr₃: lead-free nanocrystals with high photoluminescence quantum yield and picosecond radiative lifetime, ACS Mater. Lett. 3 (2021) 290–297, https://doi.org/10.1021/acsmaterialslett.0c00603.
- [3] M. Li, J. Zhou, G. Zhou, M.S. Molokeev, J. Zhao, V. Morad, M.V. Kovalenko, Z. Xia, Hybrid metal halides with multiple photoluminescence centers, Angew. Chem., Int. Ed. 58 (2019) 18670–18675, https://doi.org/10.1002/anie.201911419.
- [4] Y. Qin, P. She, X. Huang, W. Huang, Q. Zhao, Luminescent manganese(II) complexes: synthesis, properties and optoelectronic applications, Coord. Chem. Rev. 416 (2020), 213331, https://doi.org/10.1016/j.ccr.2020.213331.
- [5] T. Jiang, W. Ma, H. Zhang, Y. Tian, G. Lin, W. Xiao, X. Yu, J. Qiu, X. Xu, Y. Yang, D. Ju, Highly efficient and tunable emission of lead-free manganese halides toward white light-emitting diode and X-ray scintillation applications, Adv. Funct. Mater. 31 (2021), 2009973, https://doi.org/10.1002/adfm.202009973.
- [6] C. Li, Z. Luo, Y. Liu, Y. Wei, X. He, Z. Chen, L. Zhang, Y. Chen, W. Wang, Y. Liu, X. Chang, Z. Quan, Self-trapped exciton emission with high thermal stability in antimony-doped hybrid manganese chloride, Adv. Opt. Mater. 10 (2022), 2102746, https://doi.org/10.1002/adom.202102746.
- [7] Q. Kong, B. Yang, J. Chen, R. Zhang, S. Liu, D. Zheng, H. Zhang, Q. Liu, Y. Wang, K. Han, Phase engineering of cesium manganese bromides nanocrystals with color-tunable emission, Angew. Chem., Int. Ed. 60 (2021) 19653–19659, https://doi.org/10.1002/anie.202105413.
- [8] S. Yan, W. Tian, H. Chen, K. Tang, T. Lin, G. Zhong, L. Qiu, X. Pan, W. Wang, Synthesis of OD manganese-based organic-inorganic hybrid perovskite and its application in lead-free red light-emitting diode, Adv. Funct. Mater. 31 (2021), 2100855. https://doi.org/10.1002/adfm.202100855.
- [9] M. Liu, H. Ali-Löytty, A. Hiltunen, E. Sarlin, S. Qudsia, J.-H. Smått, M. Valden, P. Vivo, Manganese doping promotes the synthesis of bismuth-based perovskite nanocrystals while tuning their band structures, Small 17 (2021), 2100101, https://doi.org/10.1002/smll.202100101.
- [10] R.A. Auerbach, G.L. McPherson, Emission dynamics from doped crystals of (CH₃)₄NMnCl₃ (TMMC): exciton trapping in a one-dimensional lattice, Phys. Rev. B 33 (1986) 6815–6820, https://doi.org/10.1103/PhysRevB.33.6815.
- [11] Y. Rodríguez-Lazcano, L. Nataf, F. Rodríguez, Electronic structure and luminescence of [(CH₃)₄N]₂MnX₄ (X=Cl, Br) crystals at high pressures by timeresolved spectroscopy: pressure effects on the Mn-Mn exchange coupling, Phys. Rev. B 80 (2009), 085115, https://doi.org/10.1103/PhysRevB.80.085115.
- [12] Y. Peng, L. Li, C. Ji, Z. Wu, S. Wang, X. Liu, Y. Yao, J. Luo, Tailored synthesis of an unprecedented Pb–Mn heterometallic halide hybrid with enhanced emission, J. Am. Chem. Soc. 141 (2019) 12197–12201, https://doi.org/10.1021/ iacs@b04829
- [13] X. Zhu, S. Meng, Y. Zhao, S. Zhang, J. Zhang, C. Yin, S. Ye, Mn²⁺–Mn²⁺ magnetic coupling effect on photoluminescence revealed by photomagnetism in CsMnCl₃, J. Phys. Chem. Lett. 11 (2020) 9587–9595, https://doi.org/10.1021/acs.inclett.002655
- [14] H. Xiao, P. Dang, X. Yun, G. Li, Y. Wei, Y. Wei, X. Xiao, Y. Zhao, M.S. Molokeev, Z. Cheng, J. Lin, Solvatochromic photoluminescent effects in all-inorganic

- manganese(II)-based perovskites by highly selective solvent-induced crystal-to-crystal phase transformations, Angew. Chem., Int. Ed. 60 (2021) 3699–3707, https://doi.org/10.1002/anie.202012383.
- [15] H. Shinhmar, C. Hogg, M. Neveu, G. Jeffery, Weeklong improved colour contrasts sensitivity after single 670 nm exposures associated with enhanced mitochondrial function, Sci. Rep. 11 (2021), 22872, https://doi.org/10.1038/s41598-021-02311-
- [16] J.-H. Wei, J.-F. Liao, X.-D. Wang, L. Zhou, Y. Jiang, D.-B. Kuang, All-inorganic lead-free heterometallic Cs₄MnBi₂Cl₁₂ perovskite single crystal with highly efficient orange emission, Matter 3 (2020) 892–903, https://doi.org/10.1016/j.matt.2020.05.018.
- [17] M. Melamud, J. Makovsky, H. Shaked, Neutron diffraction and magnetic structure of CsMnCl₃, Phys. Rev. B 3 (1971) 3873–3877, https://doi.org/10.1103/ PhysRevB.3.3873.
- [18] Y. Sozen, S. Ozen, H. Sahin, Cesium manganese chloride: stable lead-free perovskite from bulk to single layer, J. Magn. Magn Mater. 531 (2021), 167845, https://doi.org/10.1016/j.jmmm.2021.167845.
- [19] Q. Meng, L. Zhou, Q. Pang, X. He, T. Wei, J.Z. Zhang, Enhanced photoluminescence of all-inorganic manganese halide perovskite-analogue nanocrystals by lead ion incorporation, J. Phys. Chem. Lett. 12 (2021) 10204–10211, https://doi.org/ 10.1021/acs.jpclett.1c02997.
- [20] S. Wolf, S. Seidel, J. Treptow, R. Köppe, P.W. Roesky, C. Feldmann, Room-temperature synthesis of [BMIm][Sn₅O₂Cl₇] with ∞1(Sn₂OCl₂) strands in a saline [BMIm][SnCl₃] matrix, Inorg. Chem. 61 (2022) 4018–4023, https://doi.org/10.1021/acs.inorgchem.1c03763.
- [21] M. Currie, J. Estager, P. Licence, S. Men, P. Nockemann, K.R. Seddon, M. Swadźba-Kwaśny, C. Terrade, Chlorostannate(II) ionic liquids: speciation, lewis acidity, and oxidative stability, Inorg. Chem. 52 (2013) 1710–1721, https://doi.org/10.1021/ ic300241p.
- [22] Y. Chu, S. Chen, J. Zheng, Z. Li, Elimination of oxidation and decomposition by SnCl₂ in the SERS study of pyridoxine on a roughened Au electrode, J. Raman Spectrosc. 40 (2009) 229–233, https://doi.org/10.1002/jrs.2117.
- [23] K. Timmo, M. Kauk-Kuusik, M. Pilvet, V. Mikli, E. Kärber, T. Raadik, I. Leinemann, M. Altosaar, J. Raudoja, Comparative study of SnS recrystallization in molten CdI₂, SnCl₂ and KI, Phys. Status Solidi C 13 (2016) 8–12, https://doi.org/10.1002/pssc.201510082.
- [24] G. Lu, W. Xinqiang, X. Dong, X. Hairui, L. Chunxi, W. Zihao, W. Wenchuan, A spectroscopy investigation of MnHg(SCN)₄(H₂O)₂(C₄H₃NO)₂ crystals, Mater. Chem. Phys. 100 (2006) 187–192, https://doi.org/10.1016/j. matchemphys.2005.12.029.
- [25] S. Zięba, A. Mizera, K. Pogorzelec-Glaser, A. Łapiński, Proton conducting system (ImH₂)₂SeO₄·2H₂O investigated with vibrational spectroscopy, Spectrochim. Acta 180 (2017) 224–233, https://doi.org/10.1016/j.saa.2017.02.049.
- [26] L. Chen, X. Xie, T. Su, H. Ji, Z. Qin, Co₃O₄/CdS p-n heterojunction for enhancing photocatalytic hydrogen production: Co-S bond as a bridge for electron transfer, Appl. Surf. Sci. 567 (2021), 150849, https://doi.org/10.1016/j. apsusc.2021.150849.
- [27] M. Venu Rajendran, S. Ganesan, V. Sudhakaran Menon, R.K. Raman, A. Alagumalai, A. Krishnamoorthy, Cesium iodide incorporation in tin oxide electron transport layer for defect passivation and efficiency enhancement in double cation absorber-based planar perovskite solar cells, Energy Technol. 9 (2021), 2100492, https://doi.org/10.1002/ente.202100492.
- [28] Y. Wen, P. Chen, L. Wang, S. Li, Z. Wang, J. Abed, X. Mao, Y. Min, C.T. Dinh, P. D. Luna, R. Huang, L. Zhang, L. Wang, L. Wang, R.J. Nielsen, H. Li, T. Zhuang, C. Ke, O. Voznyy, Y. Hu, Y. Li, W.A. Goddard Iii, B. Zhang, H. Peng, E.H. Sargent, Stabilizing highly active Ru sites by suppressing lattice oxygen participation in

- acidic water oxidation, J. Am. Chem. Soc. 143 (2021) 6482–6490, https://doi.org/10.1021/jacs.1c00384.
- [29] Z. Wu, Q. Zhang, B. Li, Z. Shi, K. Xu, Y. Chen, Z. Ning, Q. Mi, Stabilizing the CsSnCl₃ perovskite lattice by B-site substitution for enhanced light emission, Chem. Mater. 31 (2019) 4999–5004, https://doi.org/10.1021/acs.chemmater.9b00433.
- [30] Z.-J. Li, E. Hofman, A.H. Davis, A. Khammang, J.T. Wright, B. Dzikovski, R. W. Meulenberg, W. Zheng, Complete dopant substitution by spinodal decomposition in Mn-doped two-dimensional CsPbCl₃ nanoplatelets, Chem. Mater. 30 (2018) 6400–6409, https://doi.org/10.1021/acs.chemmater.8b02657.
- [31] W.J. Mir, M. Jagadeeswararao, S. Das, A. Nag, Colloidal Mn-doped cesium lead halide perovskite nanoplatelets, ACS Energy Lett. 2 (2017) 537–543, https://doi. org/10.1021/acsenergylett.6b00741.
- [32] B. Luo, Y. Guo, X. Li, Y. Xiao, X. Huang, J.Z. Zhang, Efficient trap-mediated Mn²⁺ dopant emission in two dimensional single-layered perovskite (CH₃CH₂NH₃)₂PbBr₄, J. Phys. Chem. C 123 (2019) 14239–14245, https://doi.org/10.1021/acs.incc.9h02649
- [33] B. Vargas, D.T. Reyes-Castillo, E. Coutino-Gonzalez, C. Sánchez-Aké, C. Ramos, C. Falcony, D. Solis-Ibarra, Enhanced luminescence and mechanistic studies on layered double-perovskite phosphors: Cs₄Cd_{1-x}Mn_xBi₂Cl₁₂, Chem. Mater. 32 (2020) 9307–9315, https://doi.org/10.1021/acs.chemmater.0c03167.
- [34] Q. Liao, Q. Meng, L. Jing, J. Pang, Q. Pang, J.Z. Zhang, Highly emissive and stable Cs₂AgInCl₆ double perovskite nanocrystals by Bi³⁺ doping and potassium bromide surface passivation, J. Phys. Chem. C 125 (2021) 18372–18379, https://doi.org/ 10.1021/acs.jpcc.1c05725.
- [35] W. Jia, R.T. Brundage, W.M. Yen, Isotope effects in the multiphonon relaxation of hydrated and deuterated cesium chloromanganate (CsMnCl₃·2H₂O, 2D₂O), Phys. Rev. B 27 (1983) 41–45, https://doi.org/10.1103/PhysRevB.27.41.
- [36] X. Tang, W. Chen, Z. Liu, J. Du, Z. Yao, Y. Huang, C. Chen, Z. Yang, T. Shi, W. Hu, Z. Zang, Y. Chen, Y. Leng, Ultrathin, core–shell structured SiO₂ coated Mn²⁺-doped perovskite quantum dots for bright white light-emitting diodes, Small 15 (2019), 1900484, https://doi.org/10.1002/smll.201900484.
- [37] X. Liu, C. Ge, Z. Yang, Y. Song, A. Wang, Y. Kang, B. Li, Q. Dong, Guanidine-templated manganese halides single crystals toward efficient mechanoluminescence and photoluminescence by supramolecular interactions modulation, Adv. Opt. Mater. 9 (2021), 2100862, https://doi.org/10.1002/adom.202100862.
- [38] J. He, H. Zhao, X. Hu, Z. Fang, J. Wang, R. Zhang, G. Zheng, B. Zhou, F. Long, Synthesis, structure, and photoelectric properties of a novel 0-dimensional organic-inorganic hybrid perovskite (2-5-py)₂MnBr₄, J. Phys. Chem. C 125 (2021) 22898–22906, https://doi.org/10.1021/acs.jpc.1e07221.
- [39] S. Wang, X. Han, T. Kou, Y. Zhou, Y. Liang, Z. Wu, J. Huang, T. Chang, C. Peng, Q. Wei, B. Zou, Lead-free MnII-based red-emitting hybrid halide (CH₆N₃)₂MnCl₄ toward high performance warm WLEDs, J. Mater. Chem. C 9 (2021) 4895–4902, https://doi.org/10.1039/D1TC00632K.
- [40] M.I. Saidaminov, J. Almutlaq, S. Sarmah, I. Dursun, A.A. Zhumekenov, R. Begum, J. Pan, N. Cho, O.F. Mohammed, O.M. Bakr, Pure Cs₄PbBr₆: highly luminescent zero-dimensional perovskite solids, ACS Energy Lett. 1 (2016) 840–845, https://doi.org/10.1021/acsenergylett.6b00396.
- [41] K. Wu, A. Bera, C. Ma, Y. Du, Y. Yang, L. Li, T. Wu, Temperature-dependent excitonic photoluminescence of hybrid organometal halide perovskite films, Phys. Chem. Chem. Phys. 16 (2014) 22476–22481, https://doi.org/10.1039/ C4CP03573A.
- [42] M. Kneissl, T.-Y. Seong, J. Han, H. Amano, The emergence and prospects of deepultraviolet light-emitting diode technologies, Nat. Photonics 13 (2019) 233–244, https://doi.org/10.1038/s41566-019-0359-9.